Chapter 4

Application of BEMD in Extraction of Regional and Local Gravity Anomalies Reflecting Geological Structures Associated with Mineral Resources

Yongqing Chen, Binbin Zhao, Jingnning Huang and Lina Zhang

Additional information is available at the end of the chapter

http://dx.doi.org/10.5772/intechopen.71222

Abstract

The bi-dimensional empirical mode decomposition (BEMD) method is an adaptive analysis method for nonlinear and nonstationary data. With the sifting process of BEMD, the data can be decomposed into a series of bi-dimensional intrinsic mode functions (BIMFs), which may present the relative local feature of the data. In this study, the BEMD method was successfully used for analyzing the Bouguer gravity data of Gejiu tin-copper polymetallic ore field in Yunnan Province and Tongshi gold field in Western Shandong Uplift Block to extract different-scale anomalies. In these two cases, regional and local components were separated, which can reflect the geological structures at different depths and some intrusive bodies which may be associated with mineral deposits. The results reveals the spatial distribution relationship between the different intrusive bodies and the various types of mineral deposits in the aforementioned two study area, which provide some reliable evidence for exploration of new concealed mineral deposits.

Keywords: BEMD, gravity anomaly, Gejiu tin-copper polymetallic ore field, Tongshi gold field

1. Introduction

With exhaustion of near surface mineral resources, we are forced to explore deeply for discovering new mineral resources. The exploration and evaluation of concealed mineral deposits represent a frontier in exploration for which geophysical methods are particularly well suited. Geophysical data from gravity and magnetic surveys may contain ore-forming

information from greater depths which has not been fully explored due to limitation of traditional mathematical model for extracting useful information. It is possible to extract deeper information from gravity and magnetic data by using new data processing technologies to construct more accurate geological structure models, including the dip and shape of geological bodies, which are essential in predicting deep ore targets. An effective use of gravity fields is to characterize forms, sizes, and depths, as well as masses of various geological objects and their relations to mineral resources. The most direct information acquired from gravity fields is the density of geological bodies. The high gravity indicates higher average densities than the others surrounded. Conversely, the low gravity represents low average densities.

Because of the heterogeneities in the densities of geological bodies during complicated geological processes, multiple solutions are an important problem to be focused. This nonunique correspondence will lead to difficulties in inferring deep geological structures and in delineating concealed geological objects, which need to be constrained by the intrinsic information from geology and geochemistry. On the other hand, some new efficient decomposition are required to extract more accurate anomalies information reflecting geological bodies and obtaining ore-finding evidences from field data.

The recorded data in geosciences usually exhibit nonlinearity and nonstationary due to the complexities of geological processes and the heterogeneities of geological bodies in composition and texture. The traditional methods, such as Fourier transform, cannot analyze nonlinear and nonstationary data seriously. For example, the methods based on Fourier transform are only suitable to analyze linear and stationary data. To handle this problem, Huang developed a new adaptive method for analyzing nonlinear and nonstationary data, named Hilbert-Huang transform (HHT) including empirical mode decomposition (EMD) and Hilbert spectral analysis [1]. The principle of bi-dimensional empirical mode decomposition (BEMD) developed on Huang's basis is elucidated in this chapter. A BEMD program on MATLAB platform was compiled and effectively used to handle regional and local gravity signals for the study areas. This yielded two types of significant two-dimensional intrinsic mode functions (BIMFs) characterizing gravitational components: RBIMFs and LBIMFs. The former depicts spatial distribution relationships between regional geological architectures at different depths which may reflect mantle and/or the basement swells and intrusive bodies which may be associated with mineral deposits. The latter does the spatial distribution relationships between the different intrusive bodies and the various types of mineral deposits, which provide some reliable evidences for searching for new concealed mineral deposits in study areas.

2. Principle of bi-dimensional empirical mode decomposition

The complicated data set can be decomposed adaptively into a finite number of different frequency components called two-dimensional intrinsic mode function (BIMF). These BIMFs are obtained through a sifting process which will not stop until the number of extrema of maximum (or minimum) points is equal or less than 2. Using the BEMD method, the local

high frequency oscillations can be extracted from original data set [1].The process of BEMD is similar to the one-dimensional EMD. Obviously, the two-dimensional extrema detection and the surface interpolation of envelops are more complicated than one-dimensional ones.

If $Ori(m,n)$ is defined as the original data set which can be decomposed into a finite number of bi-dimensional intrinsic mode functions (BIMFs) from high frequency to low frequency, $Ori(m,n)$ can be decomposed into a series of BIMFs and a residue:

$$Ori(m, n) = \sum_{i=1}^{t} B_i(m, n) + Res(m, n) \tag{1}$$

where the $B_i(m,n)$ is the ith BIMF component (from high to low frequency, $B_1(m,n)$, $B_2(m,n)$,…, $B_t(m,n)$), and $Res(m, n)$ is the residue. The frequency of $BIMF_1$ is higher than the other BIMFs'.

In the bi-dimensional sifting process, the neighboring window is used for detecting the extrema and the multiquadric method is used for computing the surface interpolation of envelopes to extract the BIMF [2, 3]. For each BIMF, a stopping criterion could be determined in the sifting process. Huang et al. [4] and Nunes et al. [2, 3] proposed that this could be realized by limitation of the size of the standard deviation, SD, which can be calculated based on the following formula (2):

$$SD_{ij} = \sum_{m=1}\sum_{n=1} \frac{\left| h_{j(i-1)}(m, n) - h_{ji}\left(m, n\right) \right|^2}{h^2_{j(i-1)}(m, n)} \tag{2}$$

The 2D sifting process can be influenced by the determination of SD. The number of BIMFs will increase with smaller SD. Besides, the mean value and standard deviation of the mean matrix $mean(m,n)$ of the upper and lower envelopes should be considered together. The 2D sifting process algorithm used in this study, first proposed by Nunes et al. [2, 3] and improved on the envelope interpolation in this study, is as follows (**Figure 1**):

(1) Initialization: $r_0(m, n) = Ori\ (m, n)$, and $j = 1$ is the BIMF index;

(2) Extraction of the jth BIMF component:

   (i) Initialize and make $h_0(m, n) = r_{i-1}(m, n)$, $i = 1$;

   (ii) detect all the points of local maximum ($m_{\max,i-1}$) and local minimum ($m_{\min,i-1}$) of $h_{i-1}(m, n)$ respectively;

   (iii) compute the upper (lower) envelope of the local maximum and local minimum point, respectively;

   (iv) calculate the envelope mean: $m_{i-1}(m, n) = (m_{\max,i-1}(m, n) + m_{\min,i-1}(m, n))/2$;

   (v) $h_i(m, n) = h_{i-1}(m, n) - m_{i-1}(x, y)$, $i = i + 1$;

   (vi) $h_i(m, n) = BIMF_j(m, n)$ if $h_i(m, n)$ matches the stopping criterion, then the jth BIMF is got, or

   (vii) repeat steps (ii)–(vi);

(3) $r_j(m, n) = r_{j-1}(m, n) - \mathrm{BIMF}_j(m, n)$; and

(4) Go to step (2), when the extrema number of $R_i(m, n)$ is more than 2, $j = j + 1$, or decomposition is ended.

Nunes et al. [2, 3] developed firstly the BEMD algorithm. In this study, the envelope interpolation was improved on the Nunes' method. The two-dimensional sifting process algorithm is illustrated as follows (**Figure 1**).

Huang et al. [1] defined the orthogonality of one-dimensional IMFs using any two IMFs, C_f and C_g through calculating the index of orthogonality (*IO*) based on the following formula:

$$IO_{fg} = abs\left(\sum_t \frac{C_f C_g}{C_f^2 + C_g^2}\right) \tag{3}$$

For the one-dimensional EMD method, orthogonality is supposed satisfied, if the *IO* value is less than 0.05.

In this study, we consider two IMFs as vector, and if they are orthogonal, the inner product is zero, that is, $IMF_i(t) \cdot IMF_j(t) = 0$. As is similar to one-dimensional EMD, for BEMD, if the index of orthogonality (*IO*) value is less than 0.05, we think the orthogonality is satisfied. The *IO* usually depends on the length of data. The shorter the length is, the bigger the *IO* is. Here, if we consider an m × n matrix to an m × n vector, the two-dimensional orthogonality is similar to the one-dimensional orthogonality. Here, we say this as a pseudo orthogonality for bi-dimensional data. That is:

$$IO = abs\left(\sum_{p=1}^{m}\sum_{q=1}^{n} \frac{BIMF_i(p, q)\, BIMF_j(p, q)}{BIMF_i^2(p, q) + BIMF_j^2(p, q)}\right), \tag{4}$$

where $BIMF_i(p,q)$ and $BIMF_j(p,q)$ are BIMF components. This method will decrease the error caused by the shortage of data in a given direction.

High-pass (S_{HP}), band-pass (S_{BP}) and low-pass (S_{LP}) defined by Freire and Ulrych [5] can be established in BEMD by selecting one or a few specific BIMF(s) to highlight certain features of geological bodies.

$$S_{HP}(m, n) = \sum_{i=1}^{k} B_i(m, n) \tag{5}$$

$$S_{BP}(m, n) = \sum_{i=k+1}^{p} B_i(m, n) \tag{6}$$

$$S_{LP}(m, n) = \sum_{i=p+1}^{t} B_i(m, n) + Res(m, n) \tag{7}$$

http://dx.doi.org/10.5772/intechopen.71222

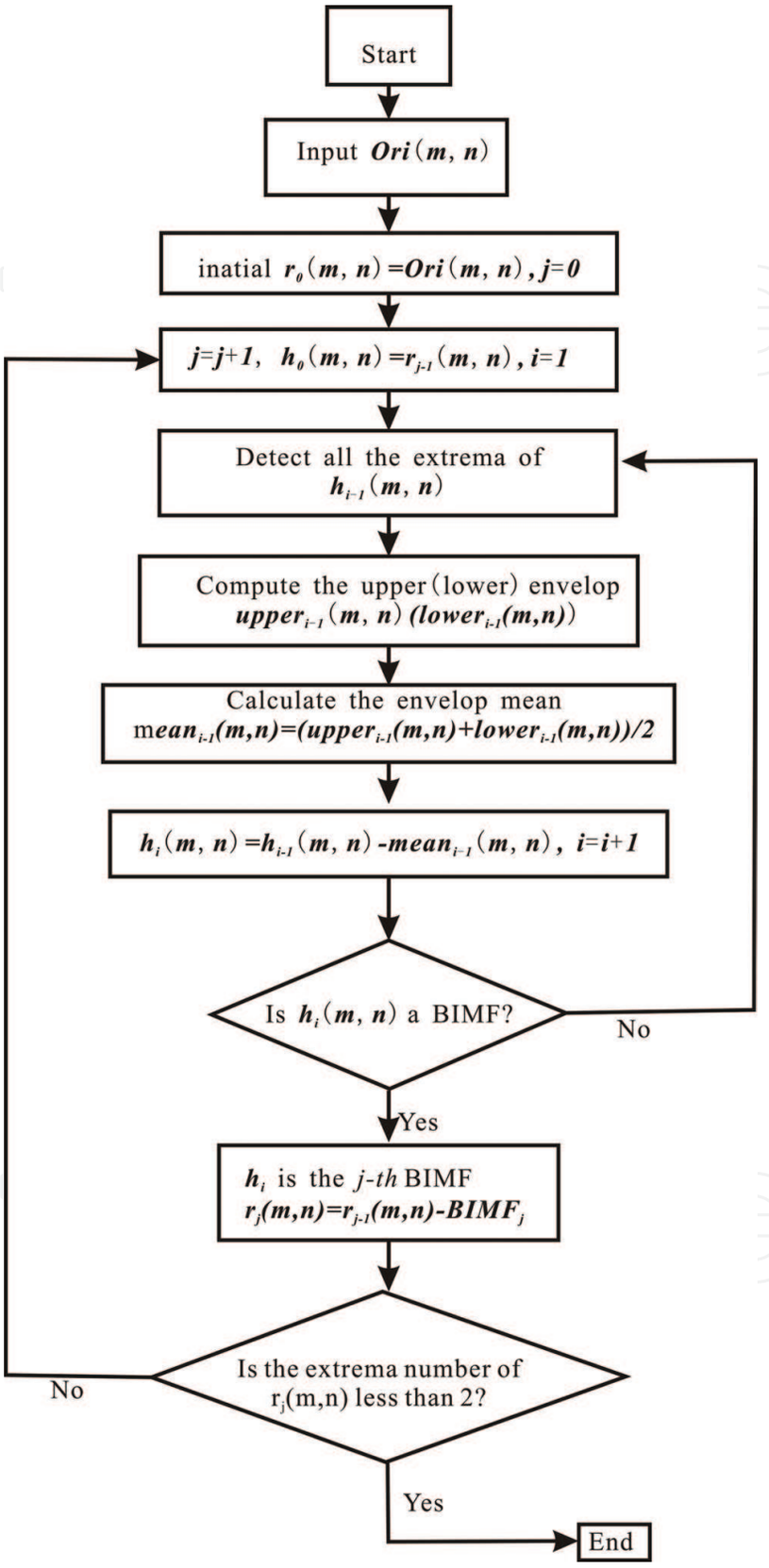

Figure 1. Sifting procedure of BEMD (revised after [2, 3]).

3. Application

3.1. Application of BEMD for extracting gravity anomalies indicating the geological architectures and granites associated mineralization in the Gejiu tin-copper polymetallic ore field

The Gejiu tin-copper polymetallic ore field, located at the westernmost end of the Cathaysia Block in South China, is one of the largest tin-polymetallic ore fields in the world. It is associated with magmatic-hydrothermal ore-forming processes triggered by deeply seated structures and concealed granites (**Figure 2**).

3.1.1. Geological background and mineralization characteristics

The world class Gejiu tin-copper polymetallic ore field is located on the western margin of the South China Block. Bounded on the northwest side by the NE-trending Mile-Shizong Fault, it is adjacent to the Yangtze Block, and bounded on the southwest side by the NW-trending ASRR Fault, it is adjacent to the Indo-China Block (**Figure 2**). The Gejiu ore field is approximately 1600 km² in area and was a tectonic sag or depression for much of its geological

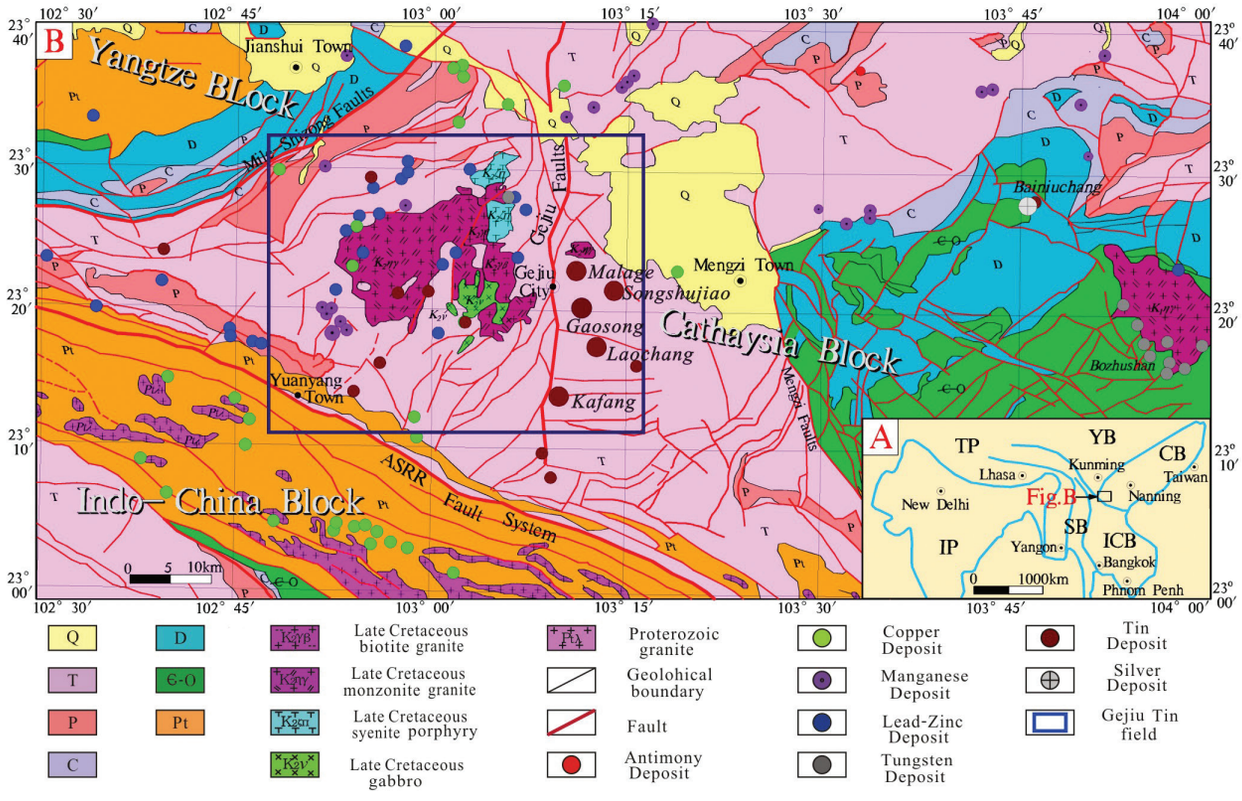

Figure 2. A: Geological outline map of southeastern Asia, showing major tectonic units and location of the Gejiu tin-copper polymetallic ore field is situated (from [6]); and B: simplified geological map showing the spatial distribution of intrusive rocks and the various types of mineral deposits in the Gejiu tin-copper polymetallic ore field and surrounding areas. CB, Cathaysia Block; YB, Yangtze Block; SB, Sibumasu Block; TP, Tibet Plate; ICB, Indo-China Block; and IP, India Plate.

history. Cambrian to Quaternary rock successions are well preserved, and the late Triassic to Cretaceous strata are preferentially exposed at the surface due to uplift associated with Yanshanian (Mesozoic) tectonic movements [7]. Most of the outcrops in the Gejiu area consist of Middle Triassic Gejiu Formation carbonates with more than 3000 m in thickness, and Middle Triassic Falang Formation fine-grained clastic sediments and carbonates with interlayering mafic lavas ranging from 1800 to 2800 m in thickness [8]. Numerous faults exist in the Gejiu area, including the NNE-trending and NE-trending faults and the NS-trending Gejiu fault (**Figure 2**). The Gejiu fault divides the Gejiu ore field into two parts (**Figure 2b**). The ore deposits are mainly located in the eastern part. Structures in the eastern part include NS-, NNE- and EW-trending faults. The EW-trending faults separate the Gejiu field into five segments from south to north, that is, Kafang, Laochang, Gaosong, Songshujiao, and Malage (**Figure 2b**). Besides Triassic lavas, the Mesozoic igneous rocks in this area can be found, for example gabbro, mafic microgranular enclave (MME)-bearing granites, porphyritic biotite granite, equigranular biotite granite, alkaline rocks and mafic dikes. SHRIMP and LA-ICP-MS zircon ages ranging from 77.4 ± 2.5 to 85.8 ± 0.6 Ma have been reported for the granitic rocks [9, 10]. The granites are transitional from metaluminous to weakly peraluminous, and are high-K and alkali-rich. Geochemical and Sr–Nd–Hf isotopic data suggest that the Gejiu granitic magma experienced high degrees of fractional crystallization following its formation due to partial melting of the Mesoproterozoic crust with minor input from mantle-derived magmas. The geochemical data indicate that the degrees of fractional crystallization are distinctive for different intrusive phases and that the later phases tend to be more evolved. These highly fractionated granites were likely generated in an intraplate setting. Mineralization is spatially related to highly evolved granitic phases. The previous studies generally suggest that the mineralization was coeval with Late Cretaceous granitic intrusions [9, 10]. The deposits in the Gejiu ore field are mostly underlain by the mid-Triassic Gejiu Formation, which consists primarily of light gray to gray limestone, with minor banded and lenticular calcareous dolomite. Greisen (quartz–muscovite), muscovite, sericite and skarn alterations were intensively developed on the margins of the cupola and in the contact zone between granite and carbonate. Skarn-sulfide ores occur along the contact zones between granite and limestone and/or dolomite, and are characterized by disseminated, veinlet and massive structures. The primary skarn minerals are pyroxene, garnet and scapolite. Tourmaline and fluorite are common hydrothermal alteration minerals overprinting skarn ores. The ores are associated with retrograde skarn minerals (actinolite, tremolite and chlorite). The major ore minerals include arsenopyrite, pyrrhotite, cassiterite, chalcopyrite and marmatite, with lesser amounts of pyrite, scheelite, native bismuth, molybdenite and magnetite [6, 11].

3.1.2. Gravity decomposition

The gravity data surveyed at a grid of 2000 m × 2000 m, covering an area including the Gejiu tin-copper polymetallic ore field and the Bozhushan silver-lead-zinc polymetallic ore field (**Figure 3**), are provided by the Yunnan Geological Survey. The total data resolution is $\pm 2.32 \times 10^{-6}$ m/s^2. The densities of the exposed geological bodies vary from 2.55 to 2.60 g/cm^3 for the granites, 2.68 to 2.72 g/cm^3 for the carbonate rocks, 2.98 to 3.10 g/cm^3 for the basic and ultrabasic rocks, and average 4.52 g/cm^3 for massive skarn tin ore within the Gejiu district [12].

In this study, a $SD = 0.02$ is assumed for decomposition of the gravity data surveyed for a grid of 2000 × 2000 m, according to the Eq. (8) using the sifting process of the BEMD described above:

$$Ori(m, n) = \sum_{i=1}^{3} B_i(m, n) + Res(m, n) \tag{8}$$

where $Ori(m, n)$ is the original 2D gravity data; $B_i(m, n)$ is the 2D IMFs; and $Res(m, n)$ is the 2D residual component. The original gravity image (**Figure 3**) was decomposed into three BIMFs ($BIMF_1$, $BIMF_2$ and $BIMF_3$) and one residue $Res(m, n)$ by BEMD. Because $BIMF_1$, $BIMF_2$ and $BIMF_3$ decrease in frequency, within the same range, $BIMF_1$ represents the gravity image with the highest frequency, and $Res(m, n)$ represents the gravity image with lowest frequency. The frequency of both the $BIMF_2$ and the $BIMF_3$ images ranges between that of $BIMF_1$ and $Res(m, n)$. The 1D decomposition results for the northeastern (line AB) and northwestern directions (line CD) of the Gejiu tin-copper polymetallic field at a mutually perpendicular angle (**Figure 3**) are shown in **Figure 4**. The smoothness of the curves increases as the frequency decreases from $BIMF_1$ to residual component. The orthogonality of the BIMFs was checked in both directions (**Table 1**). The results show that except for IO_{23} being slightly bigger than zero, IO_{12} and IO_{13} values are close to zero and thus orthogonality is approximately satisfied.

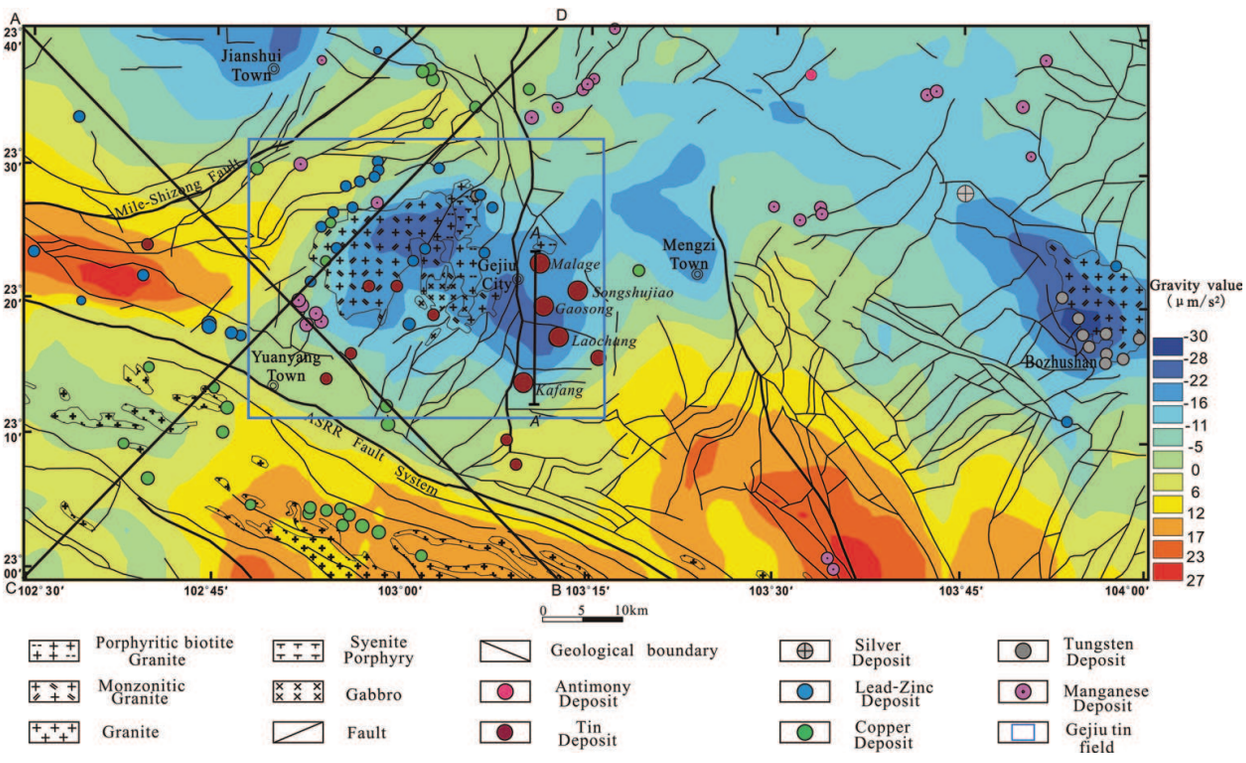

Figure 3. Original gravity image surveyed at a scale of 1:200,000 for the Gejiu tin-copper polymetallic field and surrounding areas.

http://dx.doi.org/10.5772/intechopen.71222

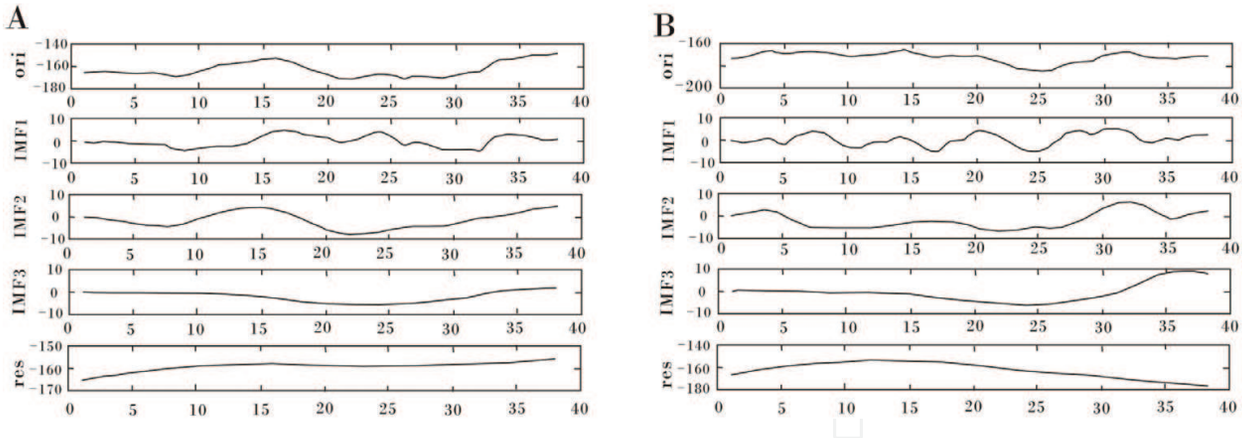

Figure 4. IMF components of 1D gravity data for the NW-trending section AB (A) and NE-trending section CD (B) shown in **Figure 3**.

Section (line)	AB	CD
IO_{12}	0.0466	0.1112
IO_{13}	0.0885	0.058
IO_{23}	0.3607	0.2996

Table 1. Orthogonality assessment.

3.1.3. Implications of the gravity decomposition components for the geology and mineralization in the Gejiu tin-copper polymetallic field

The abovementioned BIMFs have distinct geological implications. The high-pass filtered image ($BIMF_1$) depicts the shallow geological architecture in the study area (**Figure 5**). Three negative gravity anomalies bracketed by positive gravity anomalies are shown (**Figure 5**). Two among the three negative gravity anomalies correspond respectively to the outcropped granites (I) in the western Gejiu ore field and the buried granites (II) in the eastern Gejiu ore field. The positive gravity anomalies are conjectured to be created from faults filled by basic dykes and/or skarn alteration with tin-copper mineralization (IV). At the northwest side of the Gejiu ore field bounded by the NE trending Mile-Shizong fault, there is an obvious negative gravity anomaly (III) that we conjecture could be created by buried granites, which could be a new area for exploring tin-lead-zinc polymetallic deposits. A geological-geophysical profile across the whole Gejiu tin-polymetallic field from north to south (line AA′ in **Figure 5**) was drawn to show the variations of both the $BIMF_1$ gravity component and the original gravity anomaly along the geological profile (**Figure 6**). It is illustrated that the $BIMF_1$ gravity component more exactly reflects the shape fluctuation of the concealed granites, the contact metasomatic skarn alteration and tin-copper polymetallic mineralization than the original gravity anomaly and the local gravity component from

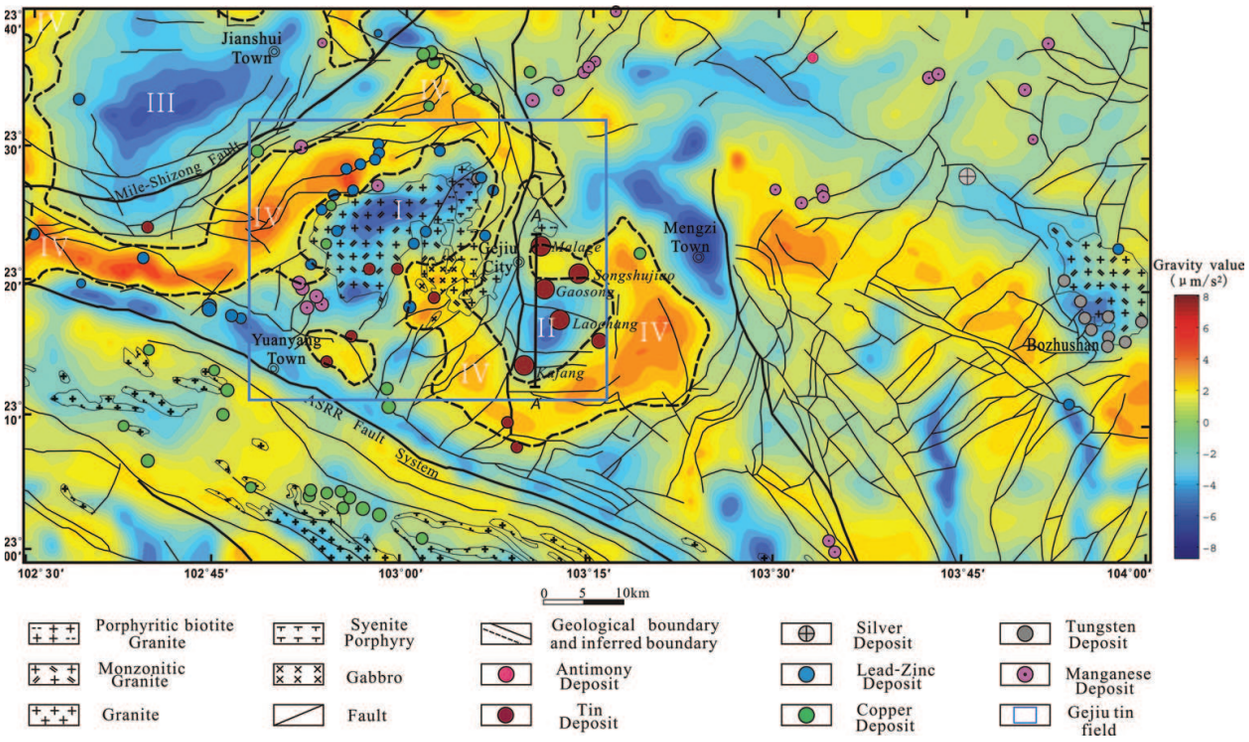

Figure 5. The gravity component $BIMF_1$ image showing that there are three negative gravity anomalies which may be associated with the tin-copper polymetallic mineralization, surrounded by rings of positive gravity anomalies which are inferred to originate from faults filled with skarn alteration and tin-copper polymetallic mineralization.

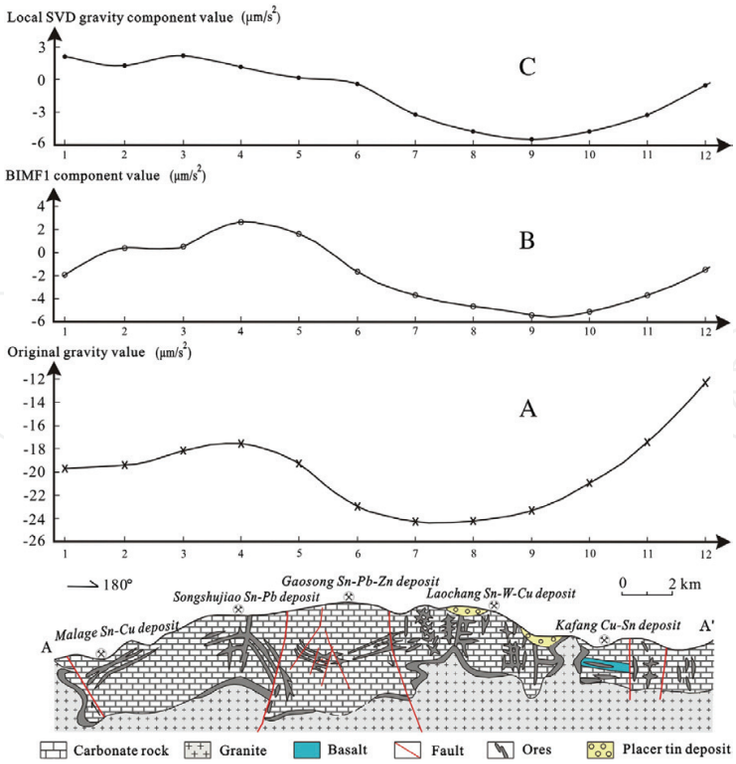

Figure 6. Spatial relationships between granites, ore bodies and local gravity components cross the section AA′ in the Gejiu tin-copper polymetallic ore field shown in **Figure 5** (modified from [10, 11]). (A) Original gravity anomaly; (B) the $BIMF_1$ gravity component decomposed from the original gravity anomaly by using BEMD; (C) local gravity component decomposed from the original gravity anomaly by using SVD [13].

http://dx.doi.org/10.5772/intechopen.71222

the singular-value decomposition (SVD) [13]. The $BIMF_1$ gravity component values vary from about –3.0 to +2.5 μm/s² from the Malaga Sn-Cu ore block toward the Songshujiao Sn-Pb ore block, in accordance with an increase in thickness of the overlying carbonate rocks, whereas from the Songshujiao Sn-Pb ore block to the Kafang Cu-Sn ore block, the IMF_1 gravity component values range from +2.5 to −5.5 μm/s², exhibiting a sharp decrease corresponding to thinning of the overlying carbonate rocks. At the south end of the section, the $BIMF_1$ gravity component values increase from −5.5 to −2.0 μm/s² in accordance with thickening of the overlying carbonate rocks (**Figure 6**). These observations imply that the local gravity anomaly variation may be mainly influenced by the shape fluctuation of the granite complex and the thickness of the overlying carbonate rock as well as local mineralization. The band-pass filtered image ($BIMF_2$) (**Figure 7**) depicts the middle-shallow geological architecture. There is a negative gravity anomaly centered area which may reflect the overall distribution of the Gejiu granitic complex, including the outcropped and the buried granites. The outcropped granites in the western Gejiu field bounded by the Gejiu fault may extend to the eastern Gejiu field at subsurface, which has been tested by drilling and mining engineering [10]. Almost all types of ore deposits are distributed around the Gejiu granitic complex displaying negative gravity anomaly, and have a close temporal-spatial relationship with the granitic complex [11].The other band-pass filtered image ($BIMF_3$) (**Figure 8**) depicts the middle-lower geological architecture. There is an EW-trending negative gravity anomaly zone (I) with two negative gravity anomaly centers (I_a and I_b) that coincide with the Gejiu tin-copper polymetallic ore field and the Bozhushan silver-lead-zinc polymetallic ore field, respectively [14, 15]. This may reflect the existence of an EW-trending granite zone at middle-low depths within the study area. The Gejiu tin-copper polymetallic ore field is

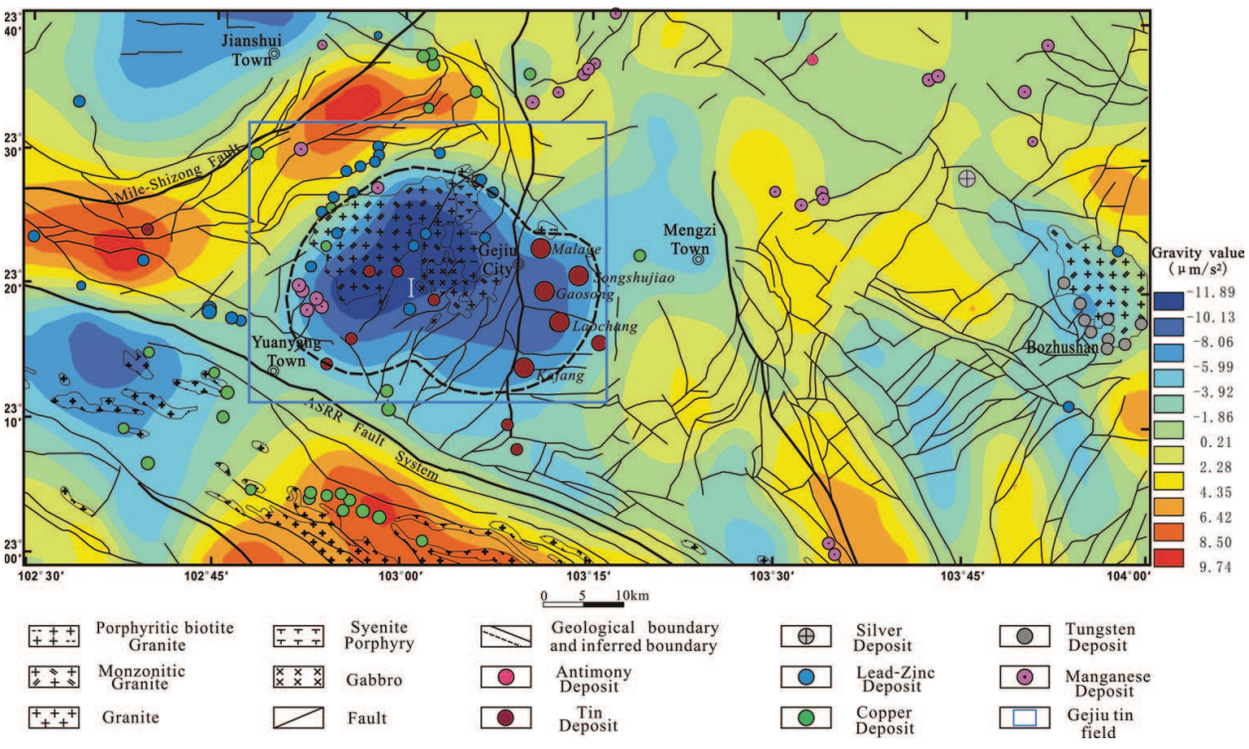

Figure 7. The gravity component $BIMF_2$ image showing a negative gravity centered area which may reflect existence of a huge granitic complex within the Gejiu tin-copper polymetallic ore field. The various ore deposits within the Gejiu tin-copper polymetallic ore field have a close spatial relationship with the granitic complex.

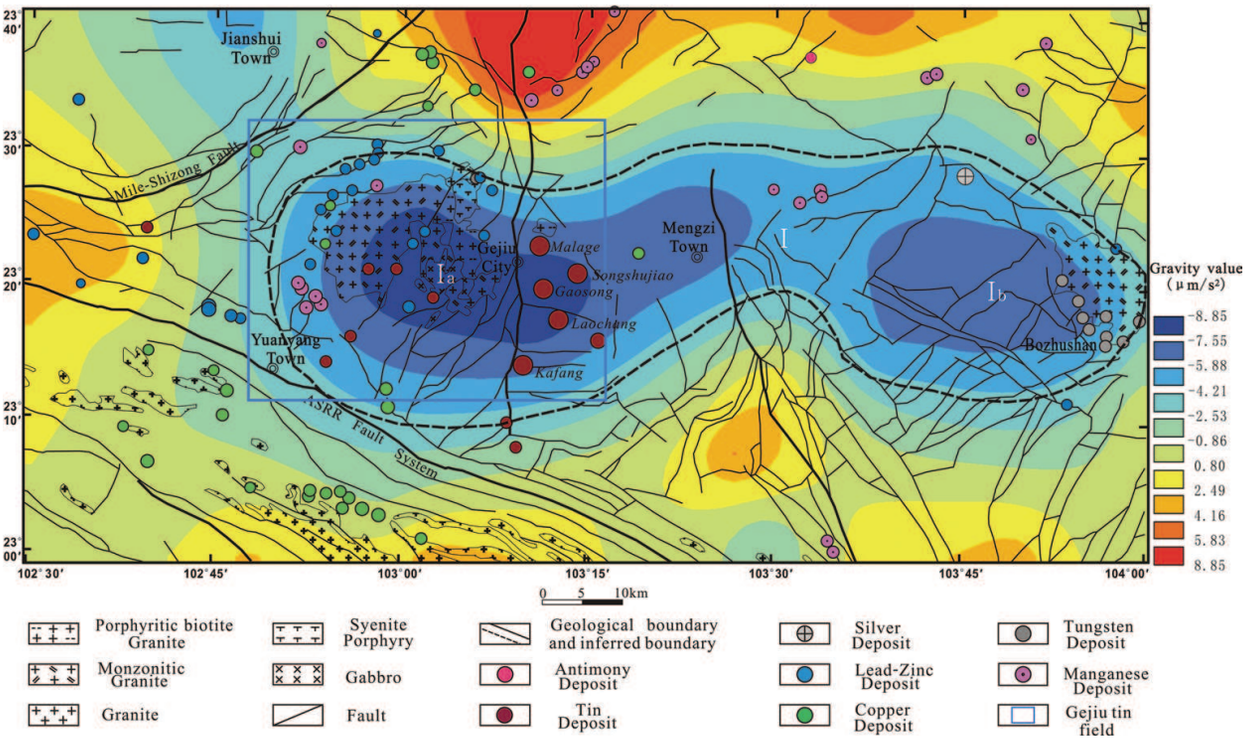

Figure 8. The gravity component $BIMF_3$ image showing an EW-trending negative gravitation anomaly zone that may reflect existence of an EW-trending granite zone connecting the Gejiu tin-copper polymetallic field to the Bozhushan silver-lead-zinc polymetallic field.

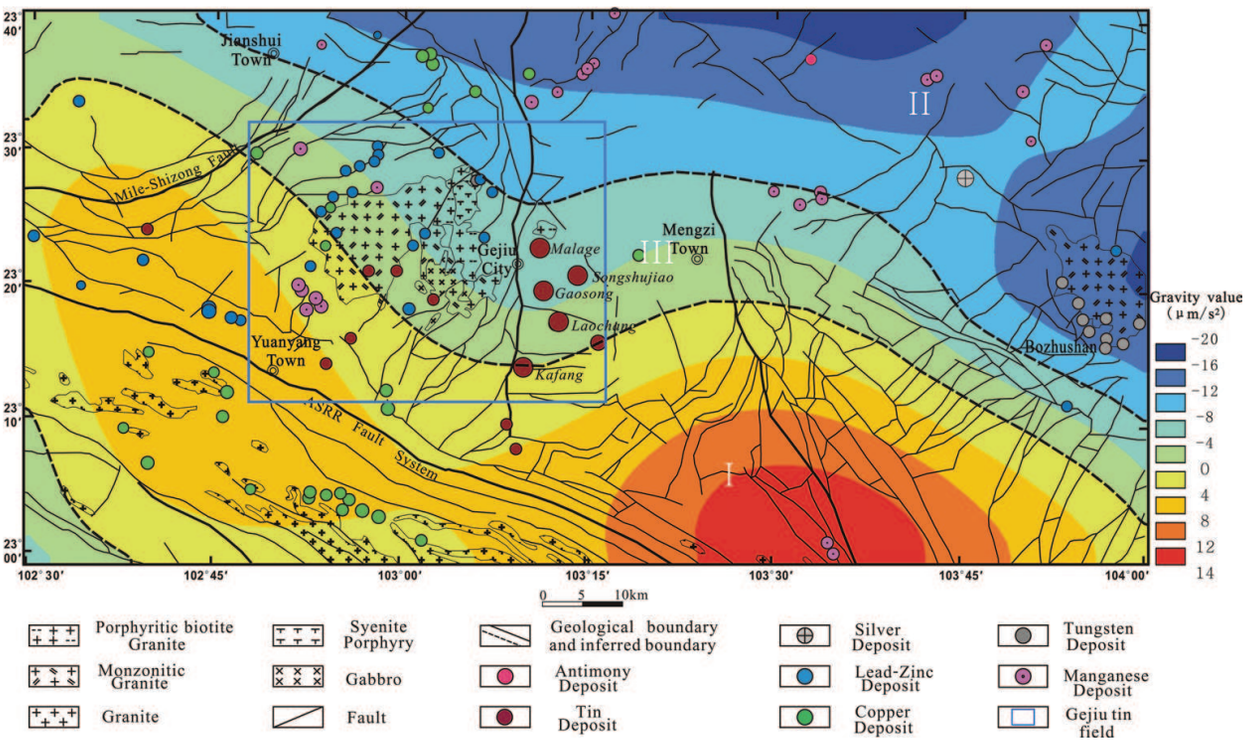

Figure 9. The residual gravity component *Res*(*m, n*) image showing the lowest geological architecture within the study area.

connected to the Bozhushan silver-lead-zinc-tin polymetallic ore field by this granite zone, forming an EW-trending regional polymetallic mineralization zone associated with the granite zone (**Figure 8**). The low-pass filtered gravity component image (*Res*(*m, n*)) (**Figure 9**) may depict the deep geological architecture within the study area, as suggested by Hou et al. [16]). In our study area, the residual map (**Figure 9**) depicts a pair of NWW-trending positive and negative gravity anomaly zones (I and II). The central axis of the positive gravity anomaly zone (I) approximately coincides with the ASRR fault which is regarded a boundary between the Indochina Block and the Cathaysia Block [17–21]. It has been illustrated that the ASRR fault cuts through the crust and controls the regional distribution of both intrusions and related mineralization [22, 23], which may have caused the mantle and/or the basement uplift with distinct positive gravity anomaly [13, 24, 25]. The negative gravity zone is inferred to be associated with the mantle and/or the basement depression (II) [13, 24–26]. The Gejiu tin-copper polymetallic deposits and the related granites that are characterized by initial $^{87}Sr/^{86}Sr$ ratios ranging from 0.7097 to 0.7130 suggesting mixed crust–mantle sources [6], are located at the transitional zone (III), whereas the Bozhushan silver-lead-zinc polymetallic deposits and the related granites with initial $^{87}Sr/^{86}Sr$ ratios ranging from 0.7126 to 0.7170 (unpublished data from authors), are situated within the zone of mantle depression. This difference in magmatic sources may be a key reason why huge amounts of tin and copper were accumulated within the Gejiu tin-copper polymetallic ore field, whereas silver, lead and zinc deposited were concentrated within the Bozhushan ore field.

3.2. Application of BEMD for extracting gravity anomalies indicating the geology and mineralization of the Tongshi gold field, Western Shandong Uplifted Block

3.2.1. Geology setting

The Tongshi gold field is located in the concealed basement to the southwestern the Mesozoic Pingyi volcanic sedimentary basin in the western Shandong Uplifted Block, Eastern China. The concealed basement area, where the Archean greenstone covered by Cambrian–Ordovician carbonates, was intruded by the Tongshi subvolcanic alkaline intrusive complex consisting of syenite porphyries and diorite porphyrites. In the Tongshi gold field, the Tongshi complex is the primary ore-controlling factor. Gold deposits (occurrences) distributed around or in the Tongshi complex can be classified into four types: (a) porphyry gold occurrences are located in the Tongshi complex, (b) Skarn iron–copper–gold deposits are located in the inner contact metasomatic zone between the intrusive complex and its host Cambrian–Ordovician carbonate rocks surrounded, (c) Crypto-breccia gold deposits and (d) Carlin-type gold deposits located in the outer contact metasomatic zone. Thus, the various types of gold deposits constitute a gold mineral resource series (**Figure 10**) [27, 28]. Two $w(^{40}Ar)/w(^{39}Ar)$ analysis of amphiboles from the diorite porphyrite and the syenite porphyry suites revealed ages of 189 and 188 Ma, respectively [29]. The intrusive complex's zircon SHRIMPU–Pb ages vary from 167.9 to 183 Ma [30]. The intrusive complex exhibits obvious negative gravity fields (**Figure 10**).

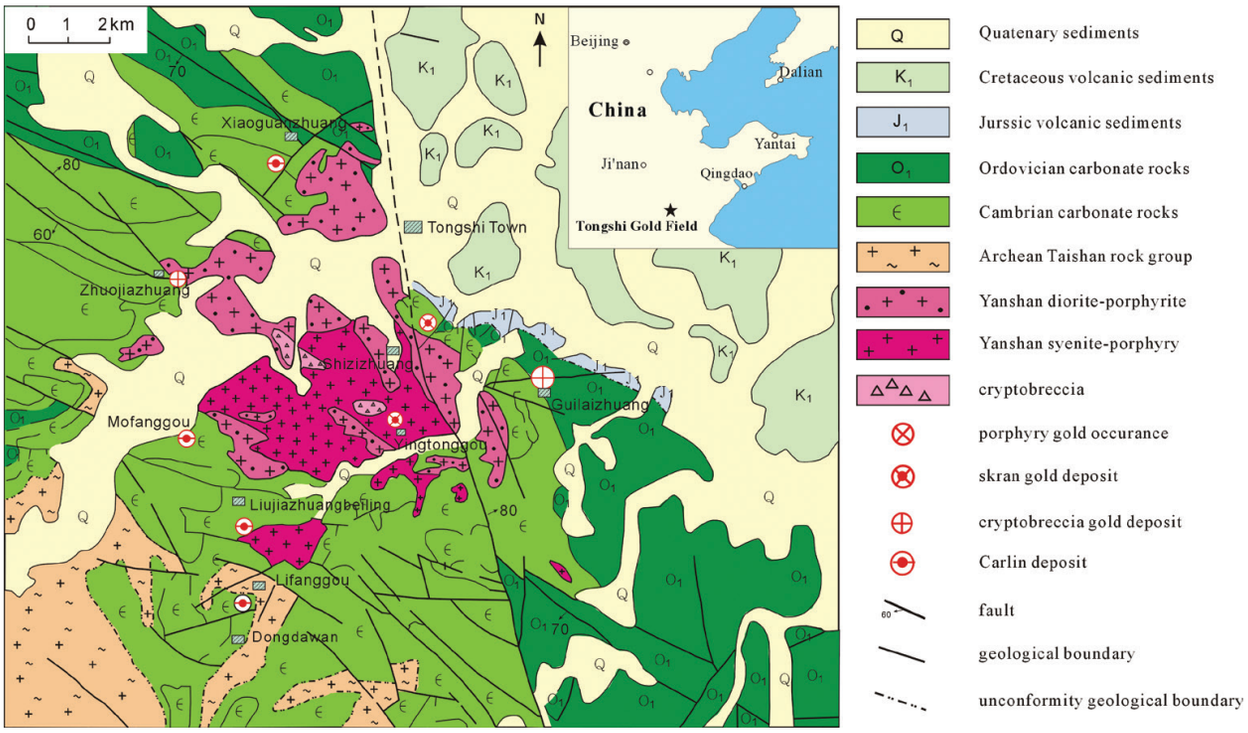

Figure 10. Geology and mineralization of Tongshi gold field, Western Shandong Uplifted Block, Eastern China (revised after [27]).

3.2.2. Gravity components decomposition

Gravity data analyzed here were surveyed at a grid of 500 m × 250 m provided by the Yanzhou Geology & Mineral Exploration Institute of Shandong province, and the study area covered about 408 km^2. The resolution of the survey data is ±2.32 × 10^{-6} m/s^2. The density of exposed geological bodies was 2.73–2.90 g/cm^3 for the Archean greenstone belt, 2.64–2.76 g/cm^3 for Cambrian–Ordovician carbonates, 2.61–2.71 g/cm^3 for the Tongshi intrusive complex and 2.46–2.53 g/cm^3 for volcanic sedimentary rocks [31]. The Bouguer gravity data (**Figure 11**) can be separated to five BIMFs (BIMF$_1$, BIMF$_2$, BIMF$_3$, BIMF$_4$ and BIMF$_5$) and a residual component *Res*(*m*, *n*) with sifting processes

$$Ori(m, n) = \sum_{i=1}^{5} BIMF_i(m, n) + Res(m, n) \quad (9)$$

where Ori(*m*, n) is the original 2D Bouguer anomaly data; BIMF$_i$(*m*, *n*) is the 2D IMFs and *Res*(*m*, *n*) is the 2D residual component. The BIMFs represent 2D gravity data characterizing the local feature with different scale which may reveal geological feature. Though BIMF$_1$, BIMF$_2$, BIMF$_3$, BIMF$_4$ and BIMF$_5$ decrease in frequency, the frequency of BIMF$_i$ is higher than that of BIMF i + 1 only within the same range, not in any range.

Here we set SD = 0.02 for the stopping condition. The 1D decomposition results for the northeastern (line AB) and northwestern directions (line CD) (**Figure 11**) are shown in **Figures 12** and **13**, respectively. The smoothness of the curves increases with the frequency decrease

http://dx.doi.org/10.5772/intechopen.71222

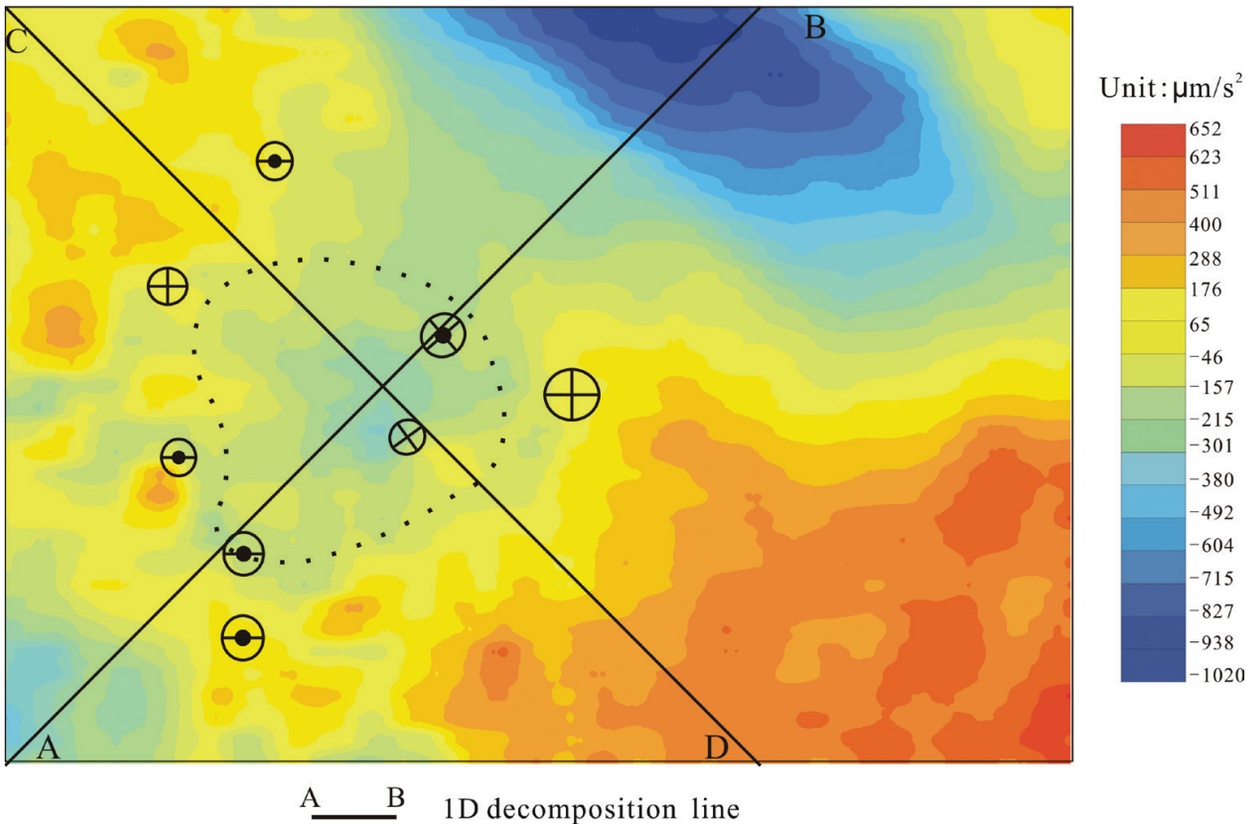

Figure 11. Original Bouguer gravity anomaly image surveyed at a scale of 1:50,000 in Tongshi gold field.

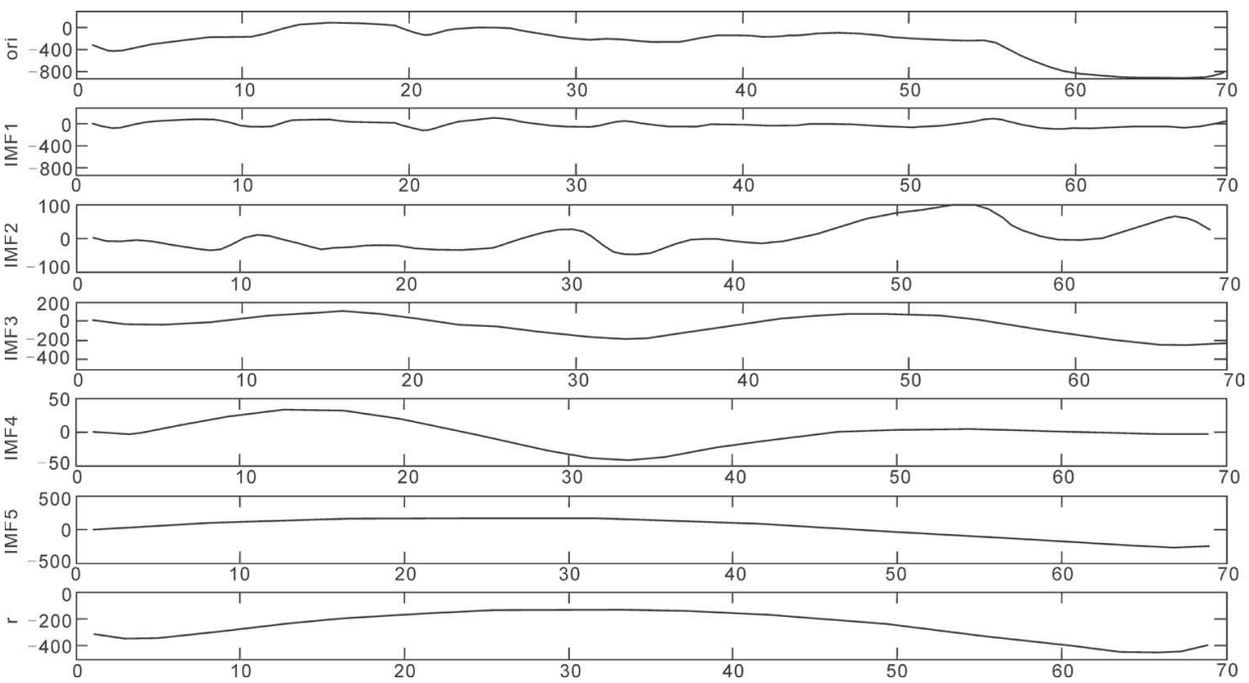

Figure 12. IMF components of one-dimensional gravity data for NE trend of a section AB shown in **Figure 11**.

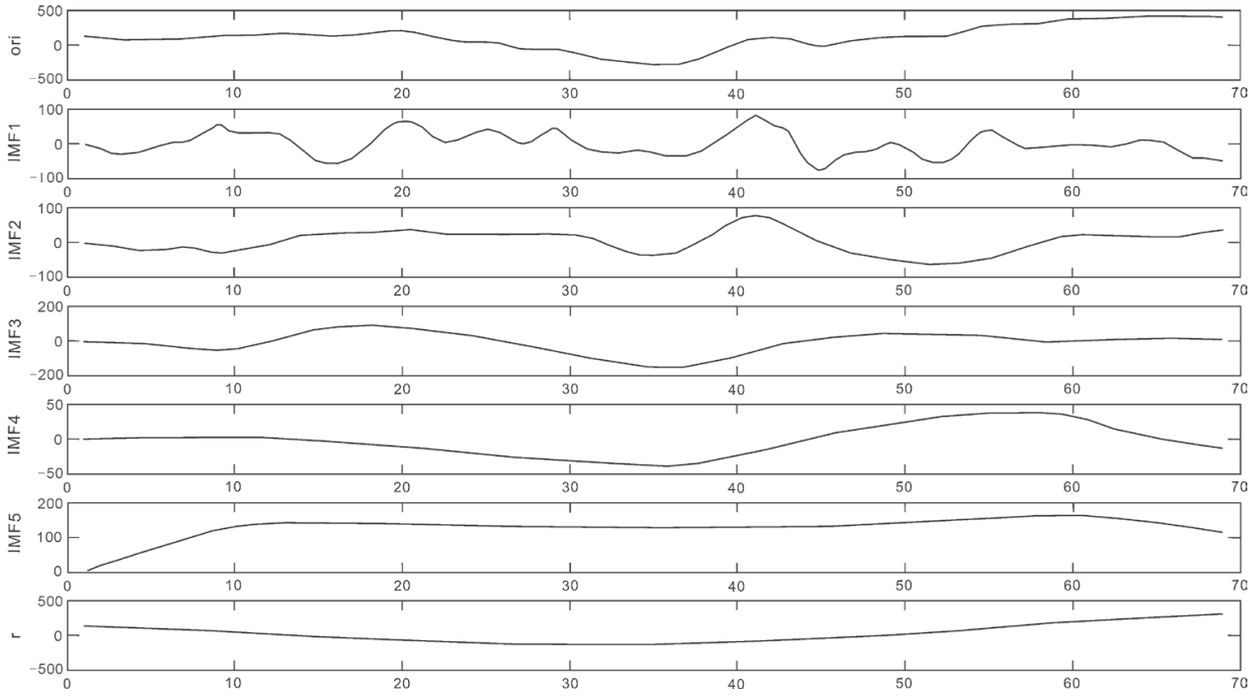

Figure 13. IMF components of one-dimensional gravity data for NW trend of a section CD shown in **Figure 11**.

from IMF_1 to IMF_5. Almost all the *IOs* we calculated are close to zero which approximately satisfied the orthogonality (**Table 2**).

3.2.3. Implications of the gravity decomposition components for the geology and mineralization in the Tongshi gold field

Both $BIMF_5$ and $BIMF_3$ components among the five BIMFs mentioned above have clear geological significance (**Figures 14** and **15**). The $BIMF_5$ image in **Figure 14** is considered as a

	Section AB	**Section CD**
IO_{12}	0.1008	0.1726
IO_{13}	0.1065	5.6550×10^{-4}
IO_{14}	0.08	0.0506
IO_{15}	0.106	0.0952
IO_{23}	0.0209	0.029
IO_{24}	0.0028	0.0245
IO_{25}	0.1426	0.014
IO_{34}	0.0954	0.0828
IO_{35}	0.1698	0.0664
IO_{45}	0.0111	0.0157

Table 2. Orthogonality assessment.

http://dx.doi.org/10.5772/intechopen.71222

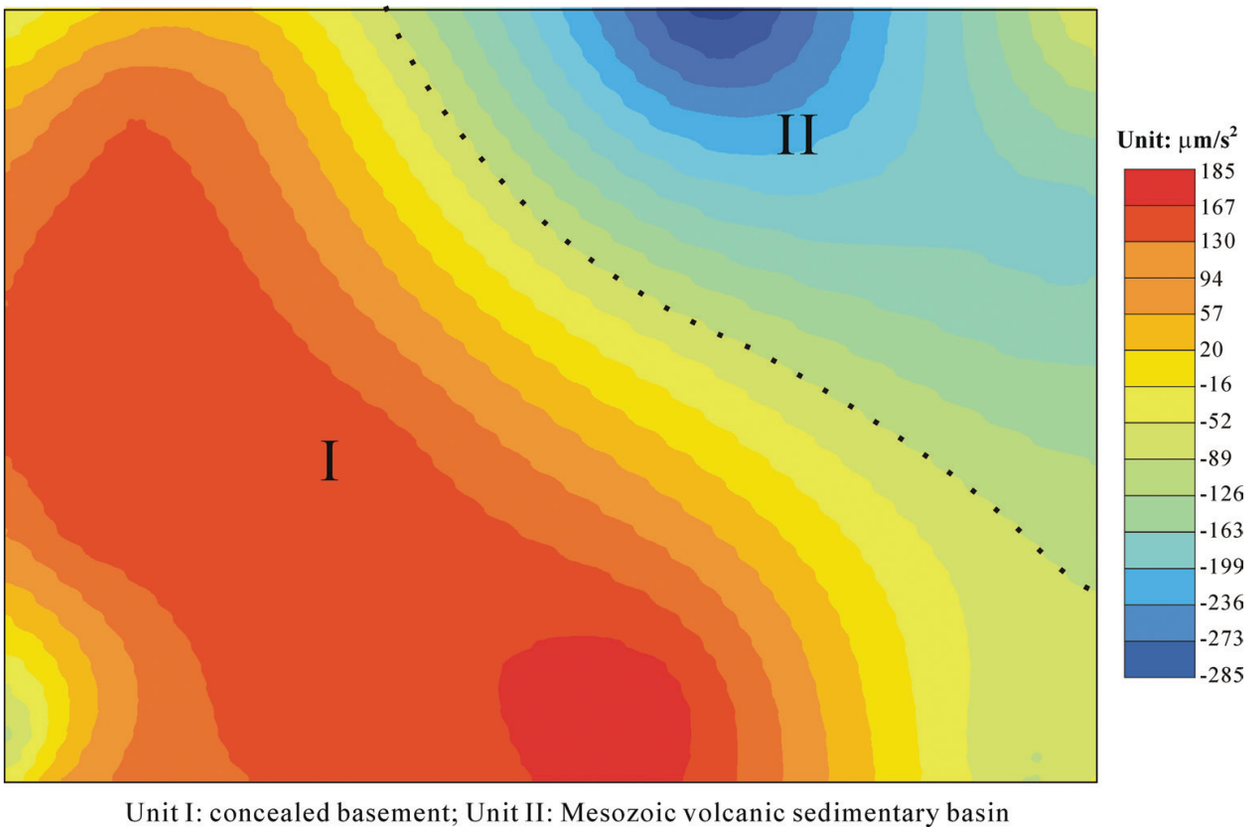

Figure 14. $BIMF_5$ image decomposed from original gravity data for Tongshi gold field.

low-pass-filtering result of the Bouguer anomaly data. Two basic deep geological units are obvious. Unit I, showing positive Bouguer anomaly, is the concealed basement with a double layer comprising Archean greenstone covered by Cambrian–Ordovician carbonate rocks. Unit II, with an obvious negative Bouguer anomaly, is the Mesozoic volcanic sedimentary basin that consists of Jurassic and the Cretaceous volcanic-sedimentary rocks. The $BIMF_3$ image (**Figure 15**) is considered as a band-pass-filtering result, which clearly reveals the geological structure of the Tongshi gold field. The Tongshi gold field includes three basic geological units according to **Figure 10**. The NW Mesozoic volcanic-sedimentary basin (II) developed in the northeast area of the study area present an obvious negative Bouguer anomaly. The Tongshi intrusive complex (III) intruded into the concealed basement exhibits relative negative gravity anomaly comparing to the host rocks.

According to its gravity anomaly features, Unit III can be subdivided into subunits IIIa, obvious negative anomalous center reflecting the distribution of Tongshi intrusive complex, and IIIb, circular positive gravity anomaly representing the contact metasomatic zone between the Tongshi intrusive complex (IIIa) and its host rocks. The spatial distributions of various types of gold deposits are controlled by Unit III (**Figure 15**).

Taking a geological section along the line EF in **Figure 15** yields a geological-geophysical pattern for the Tongshi gold field showing the formation and distribution of gold deposits (**Figure 16**). During 168–189 Ma, the Tongshi intrusive complex (IIIa), with the negative Bouguer anomaly varying from −2 to −265 μm/s², intruded into the concealed basement.

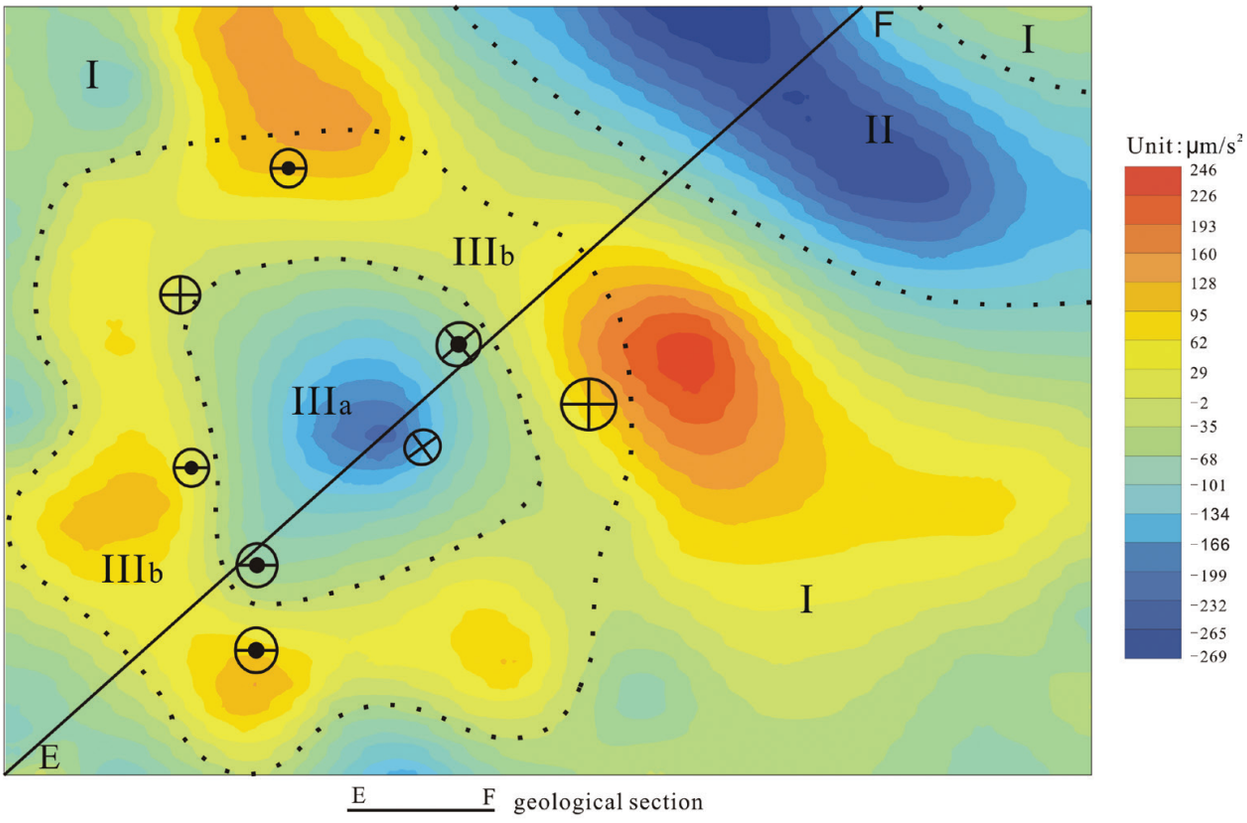

Unit I: concealed basement; Unit II: Mesozoic volcanic sedimentary basin; Unit IIIa: Tongshi intrusive complex; Unit IIIb: contact metasomatic zone between the Tongshi intrusive complex and its host rocks

Figure 15. $BIMF_3$ image decomposed from original gravity data for Tongshi gold field.

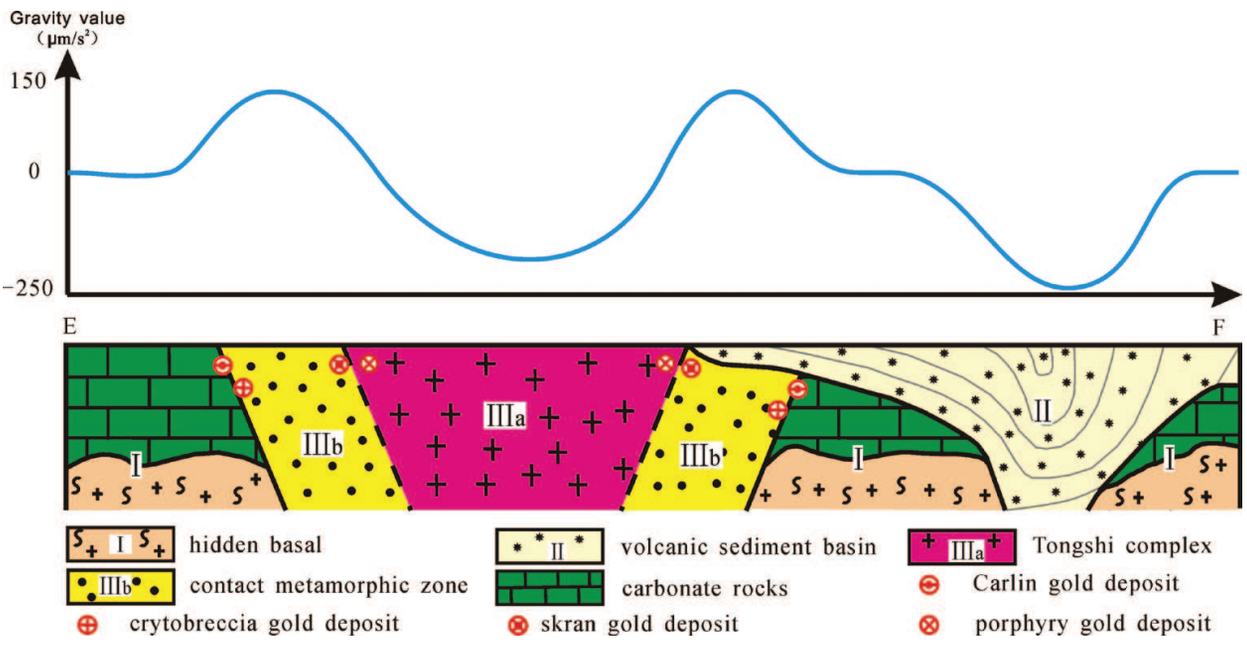

Figure 16. Geological-geophysical model of Tongshi gold field cross section EF shown in **Figure 15**.

The extracted Bouguer anomaly of the concealed basement (I) generally varies from −100 to −2 μm/s^2. But in the northeast margin, it rapidly increases from −2 to 246 μm/s^2, possibly reflecting upwelling zones of the Archean basement. The contact metasomatic zone shows positive gravity anomalies, varying from 0 to 160 μm/s^2 (IIIb), which can be attributed to metasomatic processes when magma intruded upwards into Cambrian–Ordovician carbonates. The distribution of various types of gold deposits is controlled by Unit III and displays spatial zonation. In the Tongshi intrusive complex (IIIa), porphyry gold occurrences can be found, and Skarn iron–copper–gold occurrences are located in the inner contact metasomatic zone (IIIb). Crypto-breccia and Carlin-type gold deposits are located at the outer contact metasomatic zone (IIIb) (**Figure 16**). Some undiscovered concealed gold deposits might be found on the northeastern side of the Tongshi intrusive complex (upwelling zones of the Archean basement) and the contact metasomatic zone covered by early Cretaceous volcanic-sedimentary rocks.

4. Conclusions

BEMD can effectively extract gravity components at different wavelengths that may reflect geological architectures at different depths associated with mineralization and the related intrusions in the study areas. The components are extracted by decomposing the gravity data into different bi-dimensional intrinsic mode functions (BIMFs). The gravity components of $BIMF_1$, $BIMF_2$, and …, $BIMF_i$ and $BIMF_{i+1}$, … decrease in frequency. The residual gravity component (*Res*(*m, n*)) has the lowest frequency. These gravity components decomposed by BEMD have the distinct geological implications. For the Gejiu tin-copper polymetallic field: (a) The high-pass filtered gravity component image ($BIMF_1$) depict the shallow geological architecture within the Gejiu tin-copper polymetallic field, which indicates that the skarn alteration and tin-copper mineralization with positive gravity anomalies are distributed around the granites with negative gravity anomalies. (b) The band-pass filtered gravity component images ($BIMF_2$) depict the middle-shallow geological architecture, which indicates that the outcropped granites in the western Gejiu ore field bounded by the Gejiu fault may extend to the eastern Gejiu ore field to form an integrated granitic complex in the subsurface. (c) The other band-pass filtered gravity component images ($BIMF_3$) depict the middle-lower geological architecture, which indicates that there may be an EW-trending granite zone with negative gravity anomaly at middle-lower depth connecting the Gejiu tin-copper polymetallic field to the Bozhushan silver-lead-zinc polymetallic field, displaying the existence of an EW-trending regional polymetallic mineralization zone within the study area. (d) The low-pass filtered gravity component image (the *Res*(*m, n*)) depict the lowest geological architecture within the study area, which reflects that there may be a pair of the NW-trending uplift zone of the mantle and/or the basement with positive gravity anomaly and the depression zone of the mantle and/or the basement with negative gravity anomaly. The Gejiu tin-copper polymetallic deposits and the related granites are located at their transitional zone, but the Bozhushan silver-lead-zinc polymetallic deposits and the related granites are situated within

the depression zone, which imply that the diversity of the Late Yanshanian granites and the related polymetallic deposits in the study area may be controlled by the complexity of the crust-mantle interaction in depth.

For the Tongshi gold field, both $BIMF_5$ and $BIMF_3$ components among the five BIMFs have clear geological significance (**Figures 14** and **15**). The $BIMF_5$ image in **Figure 14** is a low-pass filtering component of the original Bouguer gravity anomaly data. Two basic deep geological units are obvious. Unit I is a concealed basement with a double layer comprising Archean greenstone with the Cambrian–Ordovician carbonate rocks laid on, characterized mainly by positive gravity anomaly, and Unit II is the Mesozoic volcanic sedimentary basin that consists of Jurassic and the Cretaceous volcanic-sedimentary rocks, with an obvious negative Bouguer gravity anomaly.

The $BIMF_3$ image in **Figure 15** is a band-pass filtering component of the Bouguer gravity anomaly, which reveals the geological structure clearly. The Tongshi gold field includes three basic geological units according to **Figure 15**, (a) a concealed basement (**I**), with positive Bouguer anomaly in **Figure 14**, for which positive Bouguer anomaly at northeast margin might be the reflection of Archean metamorphic basement swells; (b) Mesozoic volcanic-sedimentary basin (**II**) extending in NW direction exhibits an obvious negative gravity anomaly; and (c) the Tongshi intrusive complex (**III**) with negative Bouguer anomaly intruded into the concealed basement. According to the extracted Bouguer anomaly features, Unit **III** can be subdivided into subunits **IIIa** and **IIIb**. The circular positive gravity anomaly (**IIIb**) around an obvious negative anomalous center (**IIIa**) might reflect the spatial distribution of the alteration and mineralization halo of the Tongshi intrusive complex, which might represent the contact metasomatic zone that developed between the Tongshi intrusive complex and its host rocks. The spatial distributions of various types of gold deposits are controlled by Unit III (**Figure 15**).

In conclusion, BEMD was successfully applied to the decomposition of gravity data for two study areas. The BEMD method is not only suitable for analysis of gravity data, but also can be extended for analysis of the scattered data like magnetic data and exploration geochemical data.

Acknowledgements

We thank Maja Bozicevic from InTechOpen for invitation. This research was jointly funded by the NSFC Program (41672329, 41272365) and the Chinese Program for probing into deep Earth (2016YFC0600509). We also thank both Yunnan Geological Survey and Yanzhou Geology & Mineral Exploration Institute of Shandong province for providing original gravity data for this research.

Author details

Yongqing Chen[1]*, Binbin Zhao[2], Jingnning Huang[3] and Lina Zhang[4]

*Address all correspondence to: yqchen@cugb.edu.cn

1 China University of Geosciences (Beijing), Beijing, China

2 Sinomine Resource Exploration Co., LTD., Beijing, China

3 The Geological Museum of China, Beijing, China

4 Reservoir Evaluation Center, CNPC Logging Co., LTD., Xi'an, China

References

[1] Huang NE, Shen Z, Long SR, Wu MC, Shi HH, Zheng Q, Yen NC, Tung CC, Liu HH. Mint: The empirical mode decomposition and the Hilbert spectrum for nonlinear and non-stationary time series analysis. Proceedings of the Royal Society of London A. 1998;**454**:903-995

[2] Nunes JC, Bouaoune Y, Delechelle E, Niang O, Bunel P. Mint: Image analysis by bi-dimensional empirical mode decomposition. Image and Vision Computing. 2003;**21**:1019-1026

[3] Nunes JC, Guyot S, Delechelle E. Mint: Texture analysis based on local analysis of the bidimensional empirical mode decomposition. Machine Vision and Applications. 2005;**16**: 177-188

[4] Huang NE, Shen SSP. Hilbert-Huang Transform and Its Applications. Singapore: World Scientific Publishing Co. Pte. Ltd.; 2005. pp. 311

[5] Freire SLM, Ulrych TJ. Mint: Application of singular value decomposition to vertical seismic profiling. Geophysics. 1988;**53**:778-785

[6] Cheng YB, Mao JW, Spandler C. Mint: Petrogenesis and geodynamic implications of the Gejiu igneous complex in the western Cathaysia block, South China. Lithos. 2013;**175-176**:213-229

[7] Party G. Geology of Tin Deposit in Gejiu Area. Beijing: Metallurgical Industry Publishing House; 1984. p. 50-90

[8] Qin DX, Li YS. Studies on the Geology of the Gejiu Sn-Cu Deposit. Beijing: Science Press; 2008

[9] Cheng YB, Mao JW. Mint: Age and geochemistry of granites in Gejiu area, Yunnan province, SW China: Constraints on their petrogenesis and tectonic setting. Lithos. 2010;**120**:258-276

[10] Cheng YB, Mao JW, Rusk B, Yang ZX. Mint: Geology and genesis of Kafang Cu–Sn deposit, Gejiu field, SW China. Ore Geology Reviews. 2012;**48**:180-196

[11] Cheng YB, Mao JW, Chang ZS, Pirajno F. Mint: The origin of the world class tin-polymetallic deposits in the Gejiu field, SW China: Constraints from metal zoning characteristics and ^{40}Ar–^{39}Ar geochronology. Ore Geology Reviews. 2013;**53**:50-62

[12] Xiong GC, Shi ST. Mint: Physico-geologic model of the Gejiu tin district and its application. Geological Review. 1994;**40**:19-27 (in Chinese with English abstract)

[13] Chen YQ, Zhang LN, Zhao BB. Mint: Application of singular value decomposition (SVD) in extraction of gravity components indicating the deeply and shallowly buried granitic complex associated with tin polymetallic mineralization in the Gejiu tin ore field, Southwestern China. Journal of Applied Geophysics. 2015;**123**:63-70

[14] Cheng YB, Mao JW, Chen XL. Mint: LA-ICP-MS Zircon U-Pb Dating of the Bozhushan Granite in Southeastern Yunnan Province and Its Significance. Journal of Jilin University (Earth Science Edition). 2010;**40**:869-878 (in Chinese with English abstract)

[15] Liu JS, Zhang HP, Ouyang YF, Zhang CH. Mint: Bainiuchang super-large silver-polymetallic ore deposit related to granitic magmatism in Mengz, Yunnani. J. Cent. South Univ. Technol. 2007;**14**:568-574

[16] Hou WS, Yang ZJ, Zhou YZ, Zhang LP, Wu WL. Mint: Extracting magnetic anomalies based on an improved BEMD method: A case study in the Pangxidong area, South China. Computers & Geosciences. 2012;**48**:1-8

[17] Wang XF, Metcalfe I, Jian P, He LQ, Wang CS. Mint: The Jinshajiang–Ailaoshan Suture zone, China: Tectonostratigraphy, age and evolution. Journal of Asian Earth Sciences. 2000:675-690

[18] Harrison TM, Chen WJ, Leloup PH. Mint: An early Miocene transition in deformation regime within the Red River fault zone, Yunnan, and its significance for indo-Asia tectonic. Journal of Geophysics Research. 1992;**97**:7159-7182

[19] Leloup PH, Lacassin R, Tapponnier P. Mint: The Ailaoshan-Red River shear zone (Yunnan, China). Tertiary transform boundary of Indochina, Tectonophysics. 1995;**251**:3-83

[20] Gilley LD, Harrison TM, Leloup PH, Ryerson FJ, Lovera OM, Wang JH. Mint: Direct dating of left-lateral deformation along the Red River shear zone, China and Vietnam. Journal of Geophysical Research. 2003;**108**:14-21

[21] Zhang JJ, Zhong DL, Sang HQ. Mint: Structural and geochronological evidence for multiple episodes of tertiary deformation along the Ailaoshan-Red River shear zone, southeastern Asia, since the Paleocene. Acta Geologica Sinica. 2006;**80**:79-96

[22] Liu JL, Chen XY, Wu WB, Tang Y, Tran MD, Nguyen QL, Zhang ZC, Zhao ZD. Mint: New tectono-geochronological constraints on timing of shearing along the Ailao Shan-Red River shear zone: Implications for genesis of Ailao Shan gold mineralization. Journal of Asian Earth Sciences. 2015;**103**:70-86

[23] Tran MD, Liu JL, Nguyen QL, Chen Y, Tang Song ZJ, Zhang ZC, Zhao ZD. Mint: Cenozoichigh-K alkaline magmatism and associated Cu–Mo–Au mineralization in the Jinping–Fan Si Panregion, southeastern Ailao Shan–Red River shear zone, southwestern China–northwestern Vietnam. Journal of Asian Earth Sciences. 2014;**79**:858-872

[24] Kane MF, Godson RH. Mint: Features of a pair of long-wavelength (>250km) and short-wavelength (<250km) Bouguer gravity maps of the United States. In: Hinze WJ, editor. The Utility of Regional Gravity and Magnetic Anomaly Maps. Society of Exploration Geophysicists; 1985. p. 46-61

[25] Zeng HL, Zhang QH, Li YS, Liu J. Mint: Crustal structure inferred from gravity anomalies in South China. Tectonophysics. 1997;**283**:189-203

[26] Shah AK, Bedrosian PA, Anderson ED, Kelley KD, Lang J. Mint: Integrated geophysical imaging of a concealed mineral deposit: A case study of the world-class pebble porphyry deposit in southwestern Alaska. Geophysics. 2013;**78**:317-328

[27] Chen YQ, Xia QL, Liu HG. Mint: Delineation of potential mineral resources region based on geo-anomaly unit. Journal of Earth Science. 2000;**11**(2):158-163 (in Chinese)

[28] Chen YQ, Zhao PD, Chen JG, Liu JP. Mint: Application of the geo-anomaly unit concept in quantitative delineation and assessment of gold ore targets in western Shandong uplift terrain, Eastern China. Natural Resources Research. 2001;**10**(1):35-49

[29] Lin JQ, Tan DJ. Mint: 40Ar/39Ar ages of Mesozoic igneous activities in western Shandong. Acta Petrologica et Mineralogica. 1996;**15**(3):213-220 (in Chinese)

[30] Hu HB, Mao JW, Niu SY, Li MW, Chai FM, Li YF, Liu T. Mint: Study on ore- forming fluids of the Guilaizhuang gold deposits in Pingyi, Western Shandong. Journal of Mineralogy and Petrology. 2005;**29**(1):38-44 (in Chinese)

[31] Wang SC, Liu YQ, Yi PH, Zhang YQ, Yang YH, Yang DL, Huang TL, Fan JZ, Ye SX, Dong T, Chen YQ, Ye SS. Mint: Gold Deposits and Synthetic Information Metallogenic Prognosis for Gold Deposit Concentrated Areas. Beijing, China: Geological Publishing House; 2003245pp (in Chinese)

IntechOpen